nature chemistry

SUPPLEMENTARY INFORMATION

DOI: 10.1038/NCHEM.2669

Surfactant-free single-layer graphene in water

Authors: George Bepete,[1,2] Eric Anglaret,[3] Luca Ortolani,[4] Vittorio Morandi,[4] Kai Huang, [1,2]

Alain Pénicaud[1,2*] and Carlos Drummond[1,2*]

Affiliations:

[1] CNRS, Centre de Recherche Paul Pascal (CRPP), UPR 8641, F-33600 Pessac, France.

[2] Univ. Bordeaux, CRPP, UPR 8641, F-33600 Pessac, France.

[3] Univ. Montpellier-II, Laboratoire Charles Coulomb (L2C), UMR CNRS 5521, F-34000 Montpellier, France.

[4] CNR IMM-Bologna, Via Gobetti 101, 40129 Bologna, Italy.

Description for Supplementary Movie 1

This movie shows the oxidation of graphenide dissolved in tetrahydrofuran upon exposure to air. The formation of graphene results in a darkening of the solution.

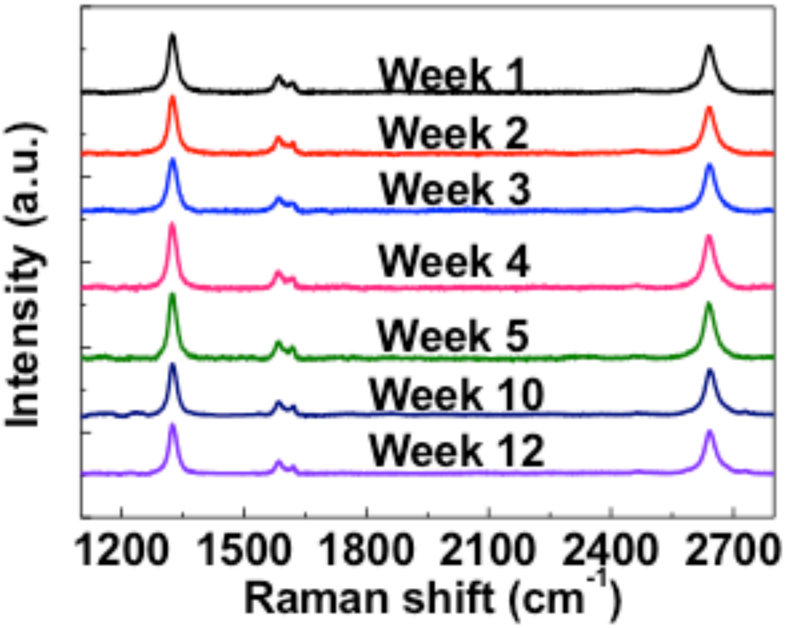

Supplementary Figure 1. Full Raman spectra (at 1.94 eV) of SLG_{iw} at different times after preparation. No evolution of the spectrum of SLG_{iw} was observed over 12 weeks of storage.

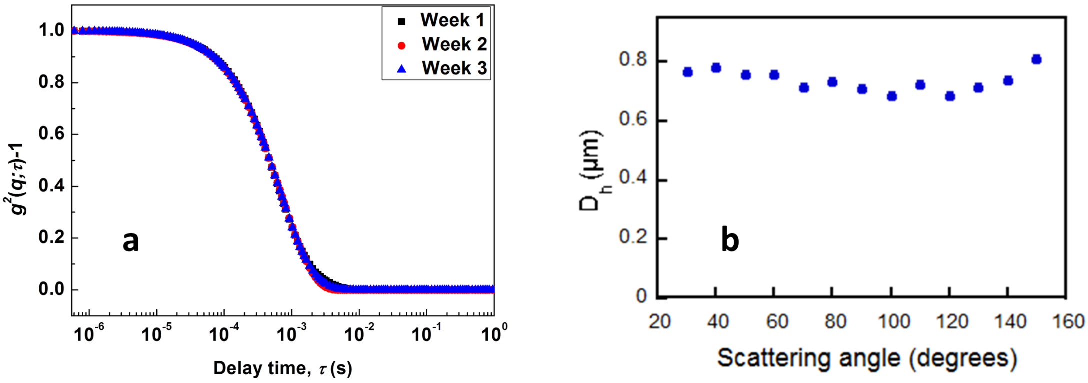

Supplementary Figure 2. a) Scattering intensity autocorrelation function ($g^2(q;\tau)$) of SLG aqueous dispersion measured at different times of storage. Scattering angle θ = 90°. No significant difference is observed with respect to the freshly prepared dispersion. b) Calculated hydrodynamic diameter D_H of graphene in water after 3 weeks of preparation, for different scattering angles. Graphene flakes have been modeled as thin disks to calculate their size from the measured decay rate of $g^2(q;\tau)$ as described before.[1] As expected, the measured size is independent of the scattering angle. As the contribution of the particles (flakes) to the measured size is weighted by the intensity of scattering (intensity distribution), larger particles have a larger weight on the calculated average than smaller particles. For this reason the measured size is significantly larger than the one obtained from AFM or SEM micrographs, which is calculated from a number distribution (each particle has equal weighting).

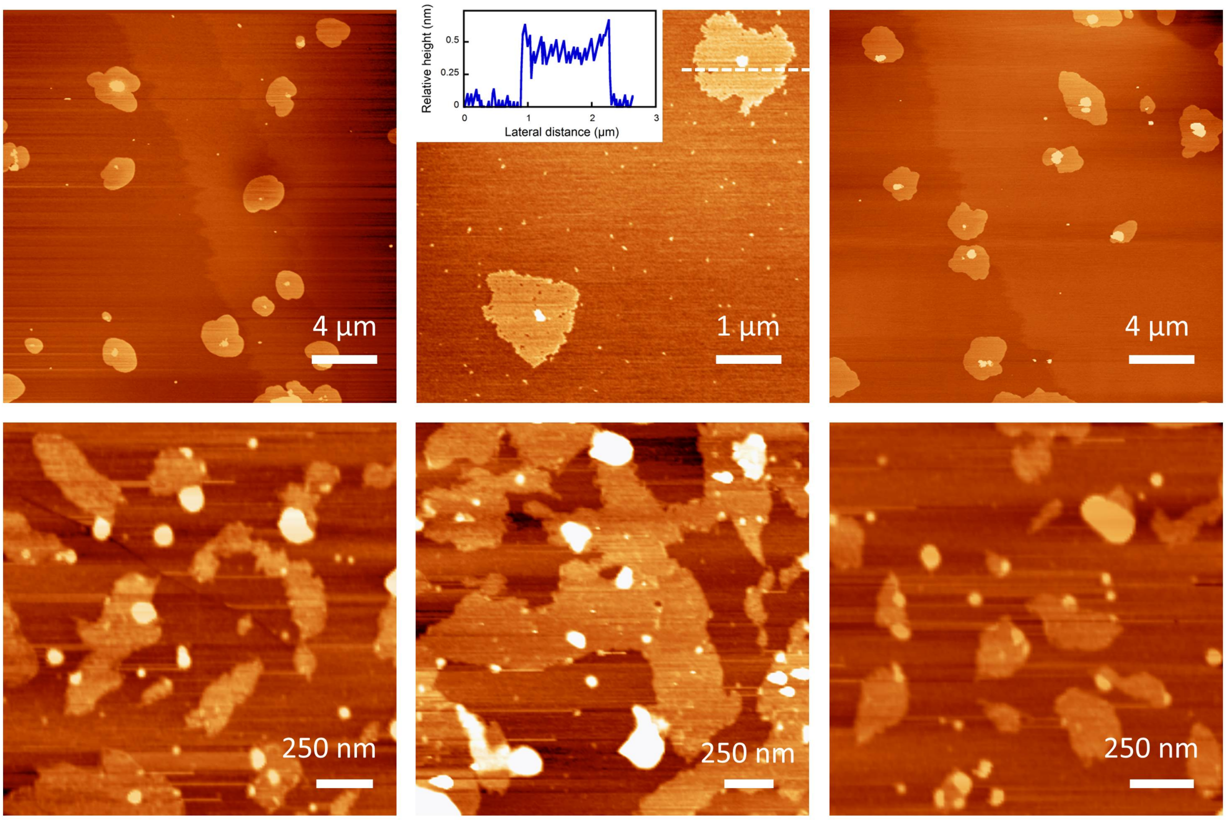

Supplementary Figure 3. Additional AFM images. The first row correspond to deposits from graphene-tetraphenyl arsonium SLG_{iw}; second row corresponds to water-only SLG_{iw}. All heights are consistent with single layer graphene.

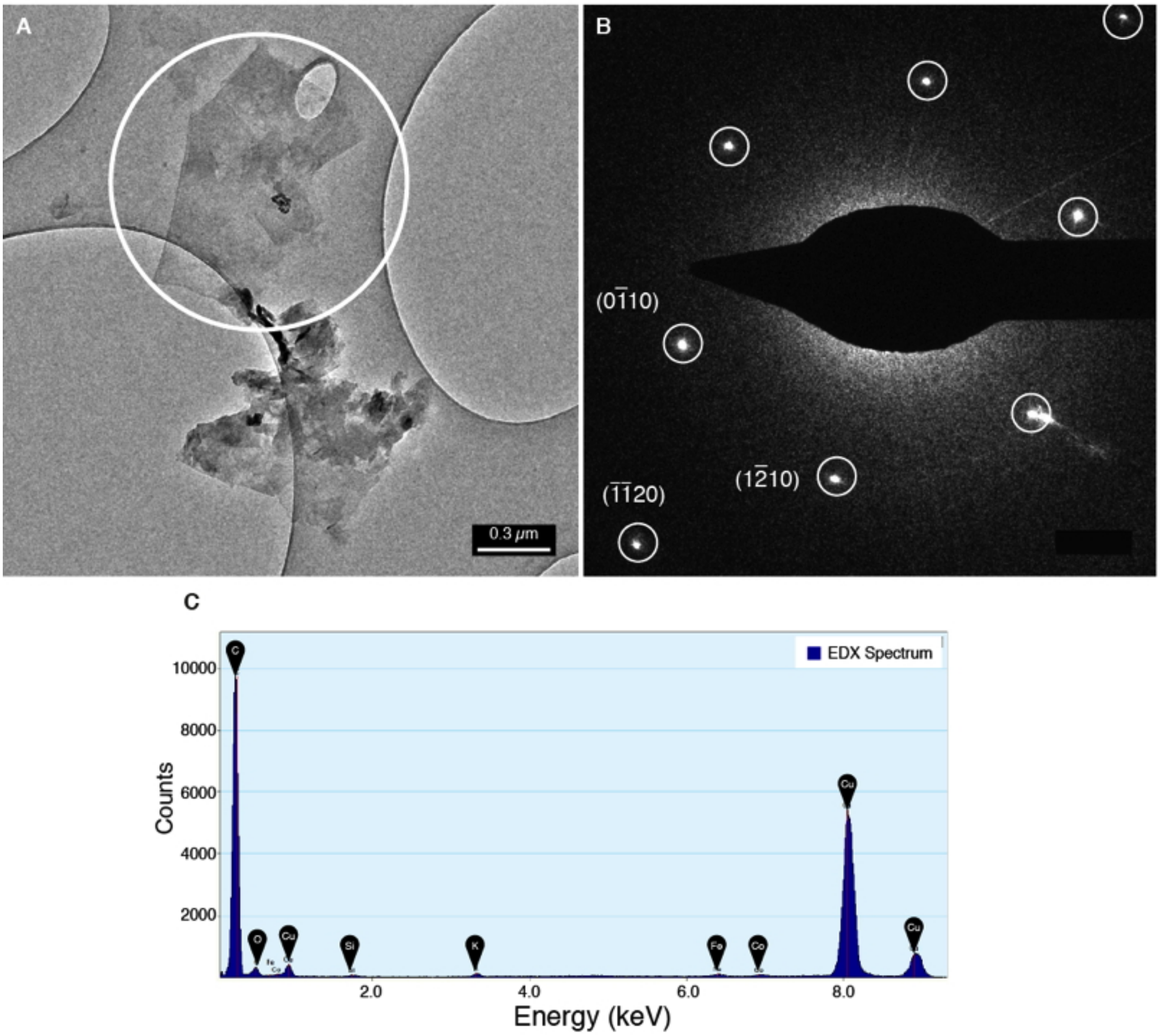

Supplementary Figure 4: Additional TEM characterization. A) TEM micrograph of a graphene flake over the amorphous carbon film of a standard TEM grid. B) Electron diffraction pattern of the region highlighted by the white circle in A. Graphite hexagonal reflections are highlighted and some crystallographic indexes are reported. The interplanar distance corresponding to the (0,-1,1,0) reflection is 0.213 nm, while the one corresponding to (-1,-1,2,0) is 0.123 nm. C) EDX spectrum acquired over the flake highlighted in A. Peaks corresponding to Si, Cu, Fe and Co comes from the TEM grid (Si and Cu) and from backscattered electrons by the polar pieces of the objective lens of the microscope.

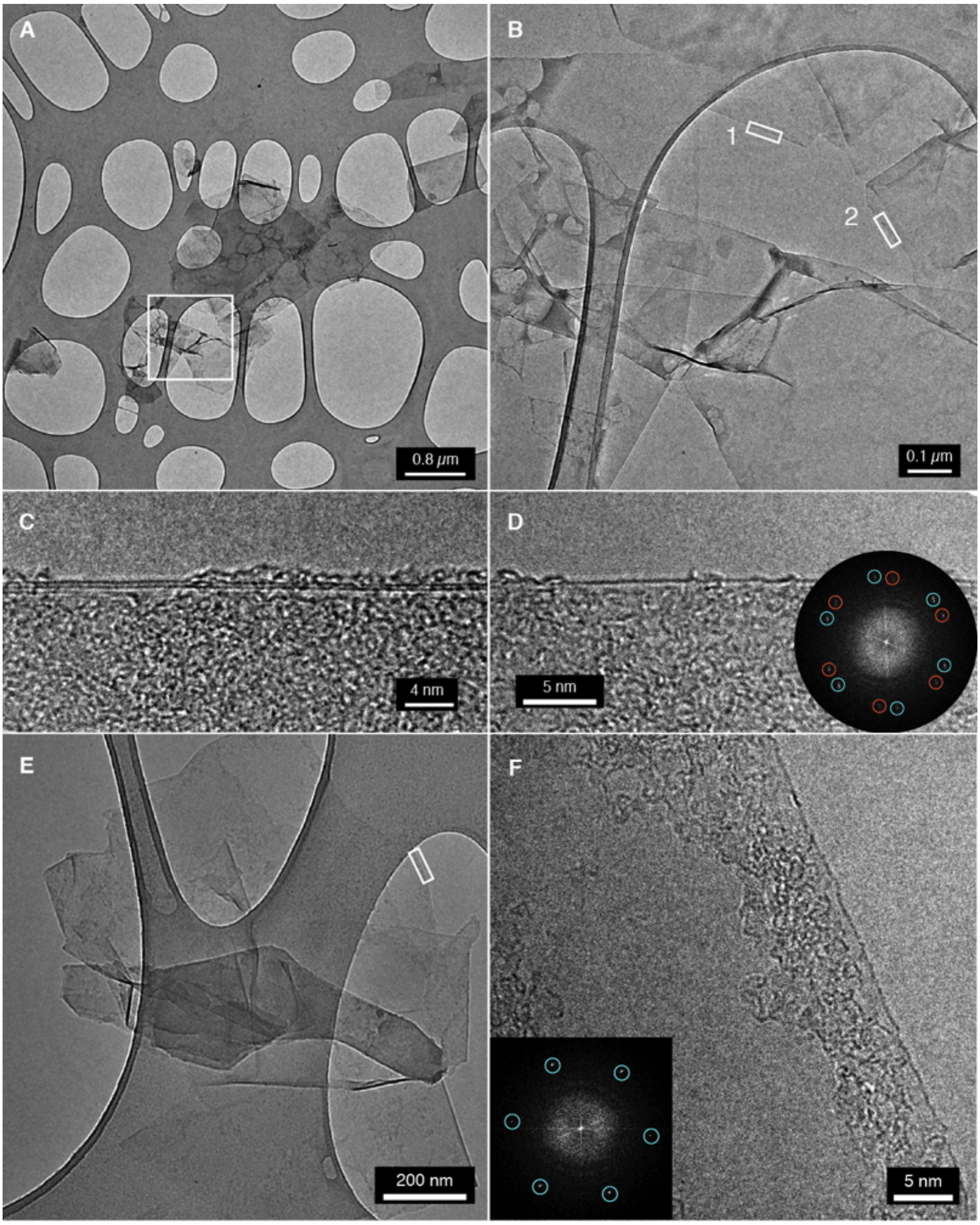

Supplementary Figure 5:Additional results of the TEM characterization of flake thickness. A) TEM micrograph of a group of graphene flakes over the amorphous carbon film of a standard TEM grid. B) Close-up of the area highlighted by the rectangle in A. C) HRTEM image of region 1 in B, showing a bilayer fold. D) HRTEM image of the region 2 in B, showing a monolayer fold. (inset) FFT of the image, showing 2 sets of hexagonal reflections (red and blue) from the folded honeycomb lattice of the flake. E) TEM micrograph of a crumpled graphene flake over the TEM grid. F) HRTEM image of the folded monolayer edge, in the region highlighted by the white rectangle in E. (inset) FFT of the image, showing the hexagonal pattern from graphene honeycomb lattice reflections.

Supplementary discussion: Graphene-graphene interaction.

Several contributions to the potential of interaction between graphene plates in water can be identified. The net balance between repulsive and attractive components will determine the stability of the graphene dispersion. Graphene flakes become electrically charged in water as a consequence of ion adsorption. The mutual repulsion due to the partial overlap of the counterion clouds is the most important contribution to the stabilizing forces. The electrostatic double layer interaction energy per unit area at distance D can be estimated as [2]

$$W(D)_{Elect} = \left({64kT\rho_\infty \left(tanh(ze\psi_0/4kT)\right)^2} \middle/ {\kappa} \right) e^{-\kappa D} \tag{1}$$

where k is Boltzmann's constant, T the absolute temperature, ρ_∞ the bulk ionic concentration, z the valence of the ions in solution, e the electron charge, ψ_0 the surface potential, and κ^{-1} the Debye length, given by $\kappa^{-1} = (\varepsilon_0 \varepsilon kT/2e^2\rho_\infty z^2)^{1/2}$, where ε is the dielectric constant of the medium and ε_0 the permittivity of free space. Calculations were performed assuming 5mM ionic concentration and ψ_0 equal to the measured graphene zeta potential (both conservative estimates).

The contribution of long-range undulation to the interparticle energy (which is not very significant for the case of graphene) can be estimated as [3],

$$W(D)_{Undul} \approx \left({(kT)^2} \middle/ {4k_b D^2} \right) \tag{2}$$

where k_b is the bending modulus of graphene [4].

Two destabilizing contributions to the total interaction energy can be identified: van der Waals and hydrophobic interactions. The van der Waals attractive energy per unit area between infinite flat plates of thickness a may be calculated as [5]

$$W(D)_{vdW} = -\frac{A_{Ham}}{12\pi}\left[\frac{1}{D^2} - \frac{2}{(D+a)^2} + \frac{1}{(D+2a)^2}\right] \tag{3}$$

where A_{Ham} is the Hamaker coefficient for the particular combination of materials. For small separations D, the non-retarded, long-wavelength limit of A_{Ham} can be used ($0.99.10^{-19}$ J for graphite-graphite in water [6]). On the contrary, the distance-dependent Hamaker coefficient is necessary for larger D values. We have used the A_{Ham} reported by Dagastine and coworkers [7] for graphite in water, which is certainly a conservative choice; it has been reported that values of A_{Ham} for graphene are substantially smaller than for graphite [8], in virtue of its two dimensional character. Thus, the actual repulsive barriers for graphene aggregation are likely to be larger than the ones calculated in this work. As it is not obvious what is the thickness for the transition of the optical properties of graphene to graphite, we have chosen to carry out the whole set of calculations using the Hamaker coefficients for graphite.

The hydrophobic interaction is probably the more difficult contribution to estimate; although it has often been observed that it decays exponentially with *D,* different values for the characteristic decay length can be found in the literature [9,10]. The authors of a recent experimental study of careful direct measurement of the hydrophobic interaction between fluid surfaces suggested the following approximation for the hydrophobic interaction [11],

$$W(D)_{hydrophobic} = -2\gamma e^{-D/D_0} \tag{4}$$

where γ is the graphene-water interfacial energy. The most difficult parameter to estimate is the decay length of the hydrophobic interaction, D_0. Tabor and coworkers reported a value of 0.3 nm [11], in agreement with the Lum-Chandler-Weeks theory [12]. However, in several studies of hydrophobic interaction between solid surfaces (in thoroughly degassed conditions) D_0 values of the order of 1 nm have been reported [9]. We have used this value in Figure 4.

The total graphene-graphene interaction energy can then be estimated simply adding the different contributions, as

$$W(D) = W(D)_{Elect} + W(D)_{Undul} + W(D)_{vdW} + W(D)_{hydrophobic} \tag{5}$$

Typical results are presented in Figure 4.

Supplementary Methods

Additional Raman characterization:

Defects in carbon materials can be conveniently analyzed and quantified by Raman spectroscopy. Graphene in SLG_{iw} can be classified as low defect « stage I » graphene according to the classification proposed by Ferrari & Robertson [13] since i) both D and G bands have narrow linewidths (27 and 21 cm^{-1}, respectively, at 2.33 eV) and ii) the linewidth of both D and 2D bands do not depend significantly on laser energy (Table S1) [14,15,13]. Furthermore, a comparison of the double resonant defect-induced bands D and D' can provide information on the nature of defects [16]. It has been shown, at 2.41 eV excitation energy, that $I_D/I_{D'}$ = 13 for *sp*^{3} type defects, $I_D/I_{D'}$ = 7 for vacancy defects, whilst $I_D/I_{D'}$ = 3.5 for edge defects (measured on polycrystalline graphite) [16]. SLG_{iw} shows a ratio $I_D/I_{D'}$ = 9 at 2.33 eV. We attribute this result to the coexistence of edge defects and *sp*^{3} defects, likely due to some functionalization of the flakes with -OH or -H groups [17,18]). The typical distance between defects, L_d, can be estimated from the I_D/I_G ratio [19,20,15]. Following the analysis of ref. [20] and considering that the structural radius for the sp^3 defects lies between the carbon-carbon distance (0.142 nm) and 1 nm [14,21], we find a typical distance between defects in the range 7-10 nm, which corresponds to a concentration of defects in the range of 300-600 ppm (detailed calculation in the next paragraph)

Excitation Energy (eV)	**D**		**G**		**D'**		**2D**		**I_D/I_G**	**$I_D/I_{D'}$**	**I_{2D}/I_G**
	ω	2Γ	ω	2Γ	ω	2Γ	ω	2Γ			
2.33	1345	27	1586	21	1620	16	2681	28	1.5	9.0	2.0
1.94	1325	26	1585	23	1617	17	2643	30	2.7	6.9	2.7
1.58	1303	28	1586	23	1612	18	2599	27	4.4	6.6	2.3
1.17	1277	34	1586	25	1605	19	2543	28	4.2	5.5	*

Supplementary Table 1. Position ω (cm^{-1}), linewidth Γ (cm^{-1}) and relevant intensity ratios as a function of excitation energy. * I_{2D}/I_G could not be measured properly at 1.17 eV because of strong absorption bands of water in the near infrared.

Estimation of the defect density

In the activation radius model, initially proposed by Lucchese *et al* [22] and developed by Cançado *et al* [20], a point defect is associated to a structural radius r_S, corresponding to the area where the structure is changed, and an activated radius r_A, corresponding to the area where the Raman D band is activated. In this model, in the limit of low defect density (with a typical distance between defects L_D>10 nm),

$$L_D^2 \approx C_A . \pi (r_A^2 - r_S^2) \left(\frac{I_D}{I_G}\right)^{-1} \tag{6}$$

where C_A corresponds to the maximum of I_D/I_G, and is therefore independent of the nature of defects, and is expressed as $C_A \approx 160 E_L^{-4}$ where E_L is the exciting laser energy. The relationship between L_D and I_D/I_G includes correcting terms for L_D<10 nm (equation 1 in reference [20]), which can be neglected in first approximation for L_D>7 nm. For Ar^+ bombardment-induced vacancy defects, r_A=3 nm and r_S=1 nm [22,20]. For sp^3 point defects, r_S could be smaller, but not smaller than the C-C distance, *i.e.* ≈ 0.142 nm. Note that several groups considered that r_S should be close for vacancies and sp^3 defects [14,21]. On the other hand, (r_A-r_S) corresponds to the correlation length of photoexcited electrons participating in the double-resonance mechanism responsible for the D band, and should be very close for all point defects. Therefore, the relation above, or in an equivalent way equation 1 in ref [20], can be used to estimate L_D from Raman measurements on SLG_{iw}. From our data measured with three different laser lines, we find L_D=6.8±1 nm if we take r_S=0.142 nm, and L_D=8.9±1 nm if we take r_S=1 nm. This leads to a defect density in the range 300-600 ppm, very close to that estimated by Hirsch et al in reference [21].

Detailed conductivity data.

Conductivity of films prepared by filtration from SLG_{iw} was measured by the 4 point method after evaporating gold contacts onto the films (Figure S6). A typical I-V curve is represented on Figure S7. Results are summarized in Table S2.

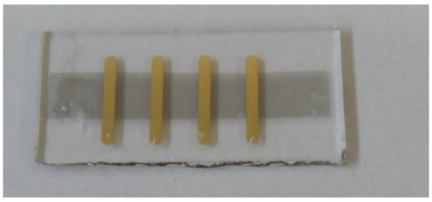

Supplementary Figure 6. Film with gold contacts evaporated on it. The distance between contacts is 4 mm.

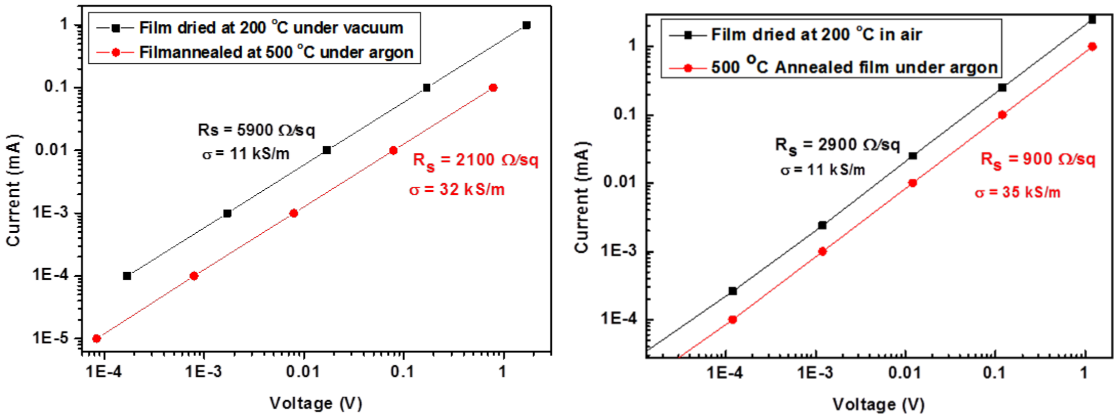

Supplementary Figure 7. Typical I-V curves obtained. Transmittance of these specific films were 65 % (left) and 35% (right).

Device	Thickness (nm)	Rs (Ω/□) 200 °C in Vac	σ (S/m) 200 °C in Vac	Rs (Ω/□) 500 °C in vac	σ (S/m) 500 °C in vac
1	35	3100	9200	820	35000
2	30	2900	11000	900	35000

Supplementary Table 2. Thickness, surface resistance and conductivity for different films prepared from SLG_{iw}

X-ray Photoelectron Spectroscopy Analysis.

Top: Survey spectrum of a film on a SiO_2 wafer (S8 top) shows prominence of the C1s peak. O peak is mostly due to contamination from the substrate since the carbon peaks show little if any C-O bonding. Bottom: C1s spectrum of a graphene film prepared from SLG_{iw} is shown in Figure S8 after drying in vacuum at room temperature and after annealing at 500 °C with comparison with graphite and a graphene film prepared by directly filtering the graphenide solution in THF. One can see that the higher energy side, indicative of sp3 carbon functionalization remains small in all cases and that annealing lowers it to the level of the film obtained from graphenide solutions

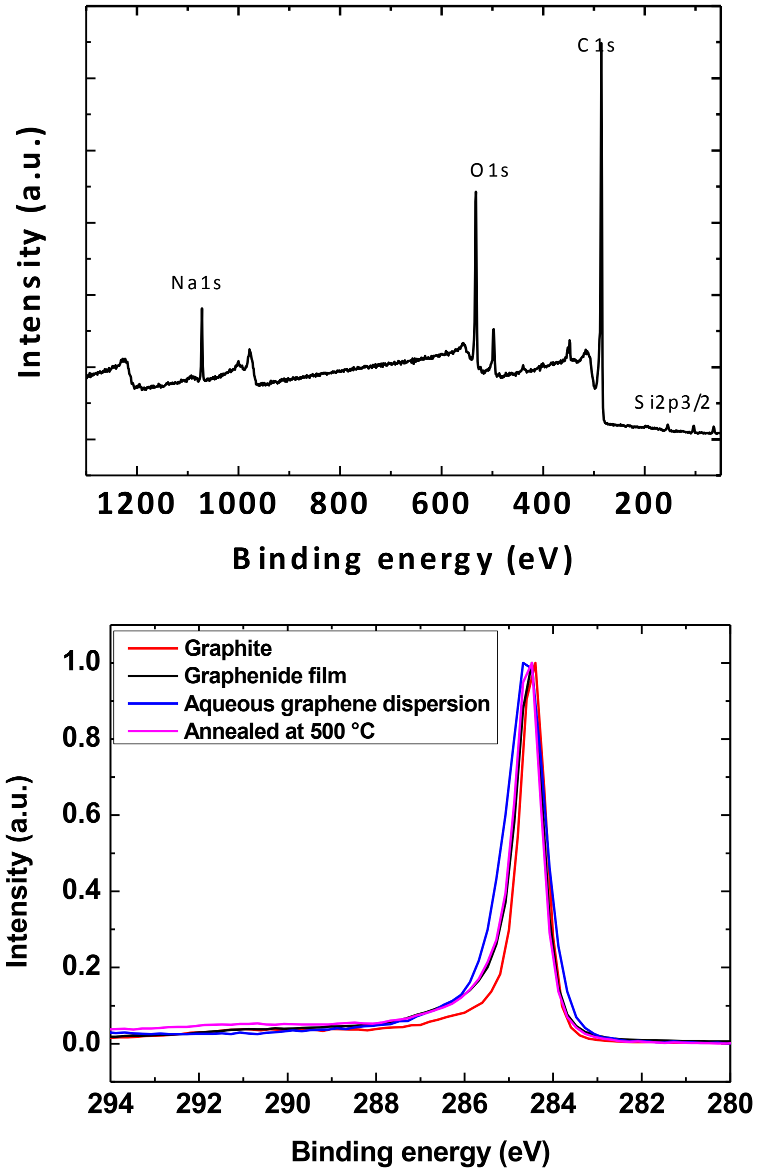

Supplementary Figure 8. Top: XPS survey spectrum of a graphene film from SLG_{iw}. Bottom : C1S spectrum of graphite (red), a graphene film obtained by filtering a graphenide solution in THF, then exposing it to air (black), a graphene film obtained from SLG_{iw} (blue) and the same film after annealing at 500 °C. RGO films, by contrast, show a series of higher energy peaks between 285 and 292 eV eV attributed to functionalized sp3 carbon atoms[23].

Comparative opacity of SLG_{iw} dispersion and sodium cholate FLG dispersions.

SLG_{iw} dispersions carefully adjusted at the same concentration as a sodium cholate FLG dispersion, show much higher transparency (Figure S9), indicating a significant difference in the nature of the two dispersions. We are now investigating the possible physical reasons for this phenomenon.

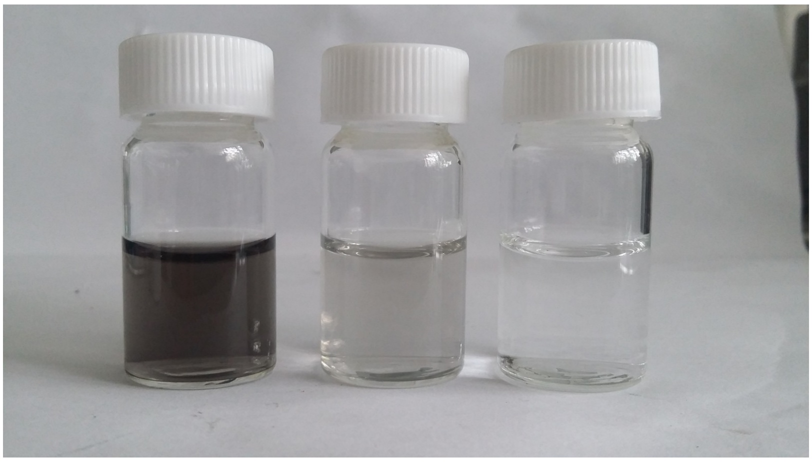

Supplementary Figure 9. Vials of Na cholate few layer graphene dispersion in water at 0.08 mg graphene/ml (left), SLG_{iw} dispersion at 0.08 mg graphene/ml (middle) and pure water (right).

Experimental procedure: The concentration of a FLG dispersion was determined by filtering a known volume of sodium cholate stabilized graphene dispersion through a nitrocellulose filter membrane (milipore, 25 nm pore size) and washing with copious amounts of water to remove sodium cholate. The nitrocellulose membrane now containing graphene was re-weighed after drying in a vacuum oven at 60 ° C for 12 hours. The sodium cholate stabilized FLG dispersion contained 0.12 mg/mL of graphene. Concentration of an SLG_{iw} sample (0.08 mg/mL) was determined using the same vacuum filtration procedure (during which the residual KOH was eliminated by the rinsing step. No residual potassium could be detected by XPS analysis). The concentration of the sodium cholate stabilized graphene dispersion was confirmed by freeze drying a known volume and weighing the remaining material. Residual mass of sodium cholate in the dried material was taken into consideration.

The sodim cholate stabilized FLG dispersion (0.12 mg/mL) was diluted to match the concentration of the SLG_{iw} sample (0.08 mg/mL).

Characterization of starting graphite.

The graphite used was natural graphite from Nacional de Grafite, Minas Gerais, Brazil. It had been previously thoroughly analyzed.[24] Flakes of lateral sizes up to a few hundred microns are seen by scanning electron microscopy (SEM) (Figure S10). Crystallite sizes La (in plane) and Lc (out of plane) have been estimated as 52 and 36 nm by Scherrer analysis of X-ray diffraction diagrams whereas La has been estimated as 145 +/- 15 nm from Raman spectroscopy.[25] XPS analysis gave the following composition : C 98.21 %, O 1.71 %, traces of Al, Mg, Fe and Si.

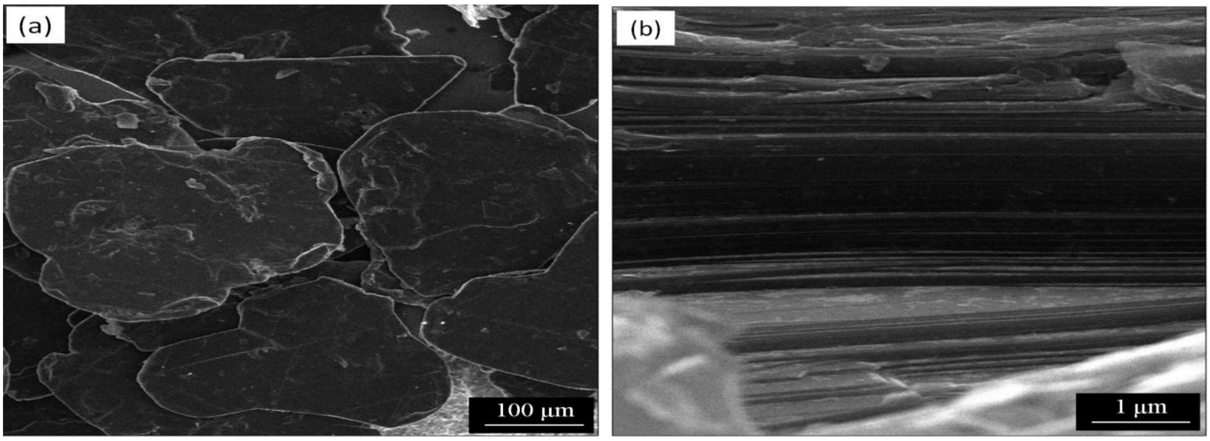

Supplementary Figure 10. Scanning electron microscopy images of natural graphite from Nacional de Grafite.

Control experiments with degassed and non-degassed water at varied pH

Attempts to prepare **SLG$_{iw}$** using non-degassed water were performed at pH between 3 and 10 (by using HCl or NaOH). In all cases the system was unstable: after few hours graphene completely separates from water. On the contrary, we have successfully prepared stable EdG in degassed water at pH between 4.5 and 11. At lower or higher pH values the charges of the graphene flakes due to ionic adsorption is too low (pH 3-4) or the ionic strength of the system is too high pH<3 or pH >11).

Atomic Force Microscopy of deposits of SLG$_{iw}$ of varied 2D linewidths.

As a control experiment, deposits were made from two different **SLG$_{iw}$** samples of varied Raman 2D linewidth. For the left image (a), the THF solution has been centrifuged at 1000 rpm before the supernatant was transferred to degassed water. Raman 2D linewidth measured in water was 37 cm^{-1}. For the right image (b), the THF solution has been centrifuged at 3000 rpm before the supernatant was transferred to degassed water. Raman 2D linewidth measured in water was below 29 cm^{-1}. The 37 cm^{-1} **SLG$_{iw}$** shows impressively well-calibrated flat flakes of mean height of ca. 1.2 nm, i.e. 4 layers whereas the single layer **SLG$_{iw}$** (2D linewidth below 29 cm^{-1}) shows rolled and crumpled flakes. We hypothesize that the different depositing behavior are due to increase rigidity with larger number of layers.

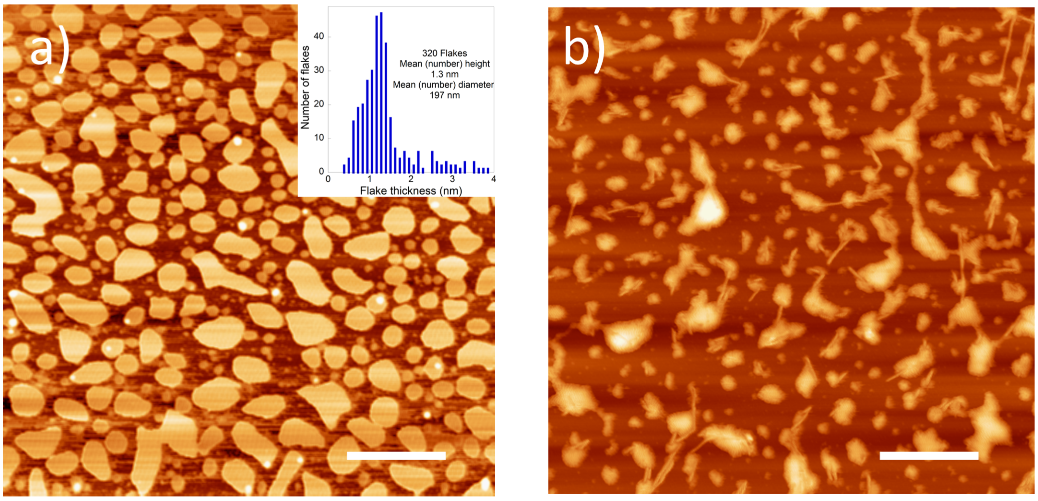

Supplementary Figure 11. AFM images of deposits of SLG$_{iw}$. Graphenide solution in THF had been centrifugated at 1000 rpm (3000 rpm) before transfer to water for image (a) ((b)) and had a 2D Raman linewidth of 37 cm^{-1} (28 cm^{-1}). Scale bar for both images is 600 nm. Statistical analysis on image (a) was performed on 320 flakes, yielding a mean (number) thickness of 1.3 nm and a thickness distribution of 1 to 6 graphene layers

X-ray diffraction characterization of films prepared from SLG$_{iw}$.

X-ray diffraction diagram of a film is plotted in Figure S12. The 002 graphitic peak is present evidencing re-stacking of the graphene layers. Interplanar distance is 3.49 Å, very close to the value for turbostratic *(uncorrelated)* packing (3.45 Å). One observes a tail at lower angle pointing to greater interplanar distances and lower packing density.

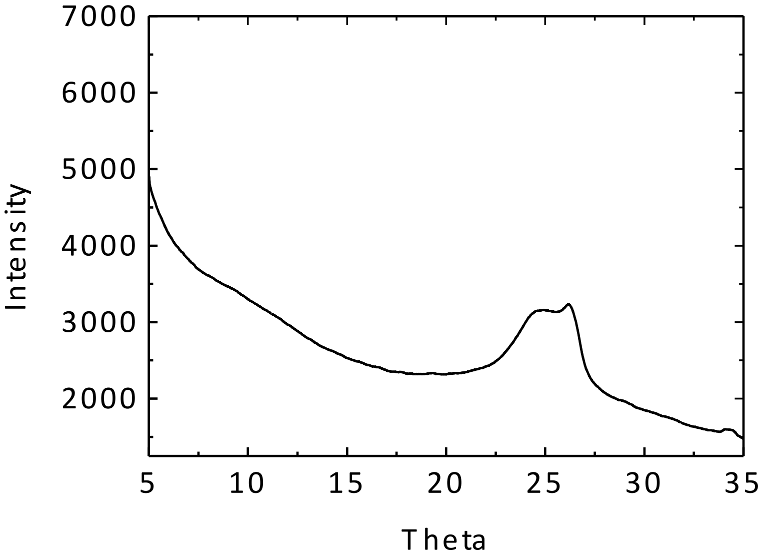

Supplementary Figure 12. X-ray diffraction diagram of a SLG_{iw} film recorded with Cu radiation (λ = 1.5418 Å).

Supplementary Note 1. About the hydrophobicity of graphene

There are at least two ways to define hydrophobicity. First, the macroscopic approach: measuring the water wettability of a surface (e.g. by contact angle) allows determining if it is more or less hydrophobic. However, this approach cannot be used at the molecular level: one couldn't measure the contact angle of water on methane or benzene. Following Kauzmann, we can define hydrophobicity at the microscopic level based on the hydrophobic interaction between species, which, e.g., determines the (unusually) low solubility of methane in water or the self-assembly of surfactant molecules.[26] Thus, hydrophobicity is a complex issue, which depends among other variables on the typical length scale of the system considered. Because of the different length scales involved (atomic and mesoscopic) graphene is placed between both worlds.

Graphite has historically been considered a hydrophobic surface (see .e.g. the reference book by Adamson and Gast[27]), and many recent reports in most prestigious journals still consider that to be the case.[28,29,30] Recent studies have reopened the debate about the actual degree of hydrophobicity of that surface. A value of ca. 65° for water contact angle on freshly cleaved, highly ordered pyrolytic graphite has recently been reported.[31] In a previous study on water wettability of the basal plane of graphite under ultrahigh vacuum, Schrader reported values between 50 and 70°.[32] Thus, pristine graphite would be rather a mildly hydrophilic substrate (from a macroscopic point of view).

The case of graphene is still being discussed in the literature. Few years ago some reports of "wetting transparency" of graphene (meaning that the wettability of a substrate covered by single layer graphene SLG remained unaltered) were published.[33] These claims have then been discussed and put in perspective.[28,34,35] In virtue of the atomic thickness of graphene, the wetting liquid (e.g. water) interacts with the supporting substrate and therefore the wetting behavior of the substrate gets partially "transmitted" to the coated surface. This ceases to be true for few layers graphene, FLG. Only few measurements of contact angle of water on suspended graphene have been reported. A very recent publication[36] reports a value of 85°. This is an interesting result: if graphene were really "wetting transparent" a value of 180° should be expected. If it were hydrophilic, a much lower angle should be anticipated. In any event, it is difficult to have a clear macroscopic approach to the wettability of graphene, as it will be affected by how/on what material graphene is supported. Thus, when we discuss the hydrophobicity of graphene in the present work, we mean it at a microscopic level. As mentioned in the main text, we are considering its disruptive effect on the H-bond formation of water which will trigger the attractive hydrophobic interaction.[12] This disruption is due to the existence of "dangling bonds" (hydrogen atoms of water molecules pointing to the graphene surface); molecules in this situation are unable to form more than 3 hydrogen bonds (to be compared to the average 3.6 H-bonds/molecule in pure water), which is unfavorable. Other than being responsible for the hydrophobic interaction, the disruptive effect of graphene promotes nanobubble nucleation on the graphene surface in water which, as described in the main text, is ultimately responsible for the instability of graphene dispersion in regular (non-degassed) water.

Supplementary References:

1. Catheline, A. *et al.* Solutions of fully exfoliated individual graphene flakes in low boiling point solvents. *Soft Matter* **8,** 7882 (2012).
2. Israelachvili, J. N. *Intermolecular and Surface Forces*. (Academic Press, 2011).
3. Servuss, R. M. & Helfrich, W. Mutual adhesion of lecithin membranes at ultralow tensions. *J. Phys.* **50,** 809–827 (1989).
4. Lu, Q., Arroyo, M. & Huang, R. Elastic bending modulus of monolayer graphene. *J. Phys. D. Appl. Phys.* **42,** 102002 (2009).
5. Parsegian, V. A. *Van der Waals Forces A Handbook for Biologists, Chemists, Engineers, and Physicists*. (Cambridge University Press, 2005).
6. Li, J.-L. *et al.* Use of dielectric functions in the theory of dispersion forces. *Phys. Rev. B* **71,** 235412 (2005).
7. Dagastine, R. R., Prieve, D. C. & White, L. R. Calculations of van der Waals forces in 2-dimensionally anisotropic materials and its application to carbon black. *J. Colloid Interface Sci.* **249,** 78–83 (2002).
8. Rajter, R. F., French, R. H., Ching, W. Y., Carter, W. C. & Chiang, Y. M. Calculating van der Waals-London dispersion spectra and Hamaker coefficients of carbon nanotubes in water from ab initio optical properties. *J. Appl. Phys.* **101,** 17–20 (2007).
9. Meyer, E. E., Rosenberg, K. J. & Israelachvili, J. Recent progress in understanding hydrophobic interactions. *Proc. Natl. Acad. Sci. U. S. A.* **103,** 15739–15746 (2006).
10. Hammer, M. U., Anderson, T. H., Chaimovich, A., Shell, M. S. & Israelachvili, J. The search for the hydrophobic force law. *Faraday Discuss.* **146,** 299–308; discussion 367–393, 395–401 (2010).
11. Tabor, R. F., Wu, C., Grieser, F., Dagastine, R. R. & Chan, D. Y. C. Measurement of the hydrophobic force in a soft matter system. *J. Phys. Chem. Lett.* **4,** 3872–3877 (2013).
12. Chandler, D. Interfaces and the driving force of hydrophobic assembly. *Nature* **437,** 640–7 (2005).
13. Ferrari, A. C. & Robertson, J. Interpretation of Raman spectra of disordered and amorphous carbon. *Phys. Rev. B* **61,** 14095–14107 (2000).
14. Eckmann, A., Felten, A., Verzhbitskiy, I., Davey, R. & Casiraghi, C. Raman study on defective graphene: Effect of the excitation energy, type, and amount of defects. *Phys. Rev. B* **88,** 035426 (2013).
15. Martins Ferreira, E. H. *et al.* Evolution of the Raman spectra from single-, few-, and many-layer graphene with increasing disorder. *Phys. Rev. B* **82,** 125429 (2010).
16. Eckmann, A. *et al.* Probing the nature of defects in graphene by Raman spectroscopy. *Nano Lett.* **12,** 3925–3930 (2012).

17. Hof, F., Bosch, S., Eigler, S., Hauke, F. & Hirsch, A. New basic insight into reductive functionalization sequences of single walled carbon nanotubes (SWCNTs). *J. Am. Chem. Soc.* **135,** 18385–18395 (2013).

18. Schäfer, R. a *et al.* On the way to graphane-pronounced fluorescence of polyhydrogenated graphene. *Angew. Chem. Int. Ed. Engl.* **52,** 754–7 (2013).

19. Ferrari, A. C. & Basko, D. M. Raman spectroscopy as a versatile tool for studying the properties of graphene. *Nat. Nanotechnol.* **8,** 235–46 (2013).

20. Canc□ado, L. G. *et al.* Quantifying Defects in Graphene via Raman Spectroscopy at Different Excitation Energies. *Nano Lett.* **11,** 3190–3196 (2011).

21. Eigler, S. & Hirsch, A. Chemistry with Graphene and Graphene Oxide-Challenges for Synthetic Chemists. *Angew. Chemie Int. Ed.* **53,** 7720–7738 (2014).

22. Lucchese, M. M. *et al.* Quantifying ion-induced defects and Raman relaxation length in graphene. *Carbon N. Y.* **48,** 1592–1597 (2010).

23. Becerril, H. A. *et al.* Evaluation of Solution-Processed Reduced Graphene Oxide Films as Transparent Conductors. *ACS Nano* **2,** 463–470 (2008).

24. Wang, Y. Graphenide Solutions and Graphene Films. (The University of Bordeaux, 2014).

25. Canc□ado, L. G. *et al.* General equation for the determination of the crystallite size L_a of nanographite by Raman spectroscopy. *Appl. Phys. Lett.* **88,** 163106 (2006).

26. Kauzmann, W. Some Factors in the Interpretation of Protein Denaturation. *Adv. Protein Chem.* **14,** 1–63 (1959).

27. Adamson, A. W. & Gast, A. P. *Physical Chemistry of Surfaces*. (1997).

28. Shih, C.-J. *et al.* Breakdown in the Wetting Transparency of Graphene. *Phys. Rev. Lett.* **109,** 176101 (2012).

29. Taherian, F., Marcon, V., van der Vegt, N. F. A. & Leroy, F. What Is the Contact Angle of Water on Graphene? *Langmuir* **29,** 1457–1465 (2013).

30. Munz, M., Giusca, C. E., Myers-Ward, R. L., Gaskill, D. K. & Kazakova, O. Thickness-Dependent Hydrophobicity of Epitaxial Graphene. *ACS Nano* **9,** 8401–8411 (2015).

31. Kozbial, A. *et al.* Understanding the intrinsic water wettability of graphite. *Carbon N. Y.* **74,** 218–225 (2014).

32. Schrader, M. E. in *Modern Approaches to Wettability* (eds. Schrader, M. E. & Loeb, G. I.) 53–71 (1992).

33. Rafiee, J. *et al.* Wetting transparency of graphene. *Nat. Mater.* **11,** 217–222 (2012).

34. Shih, C.-J., Strano, M. S. & Blankschtein, D. Wetting translucency of graphene. *Nat. Mater.* **12,** 866–869 (2013).

35. Kim, D., Pugno, N. M., Buehler, M. J. & Ryu, S. Solving the Controversy on the Wetting Transparency of Graphene. *Sci. Rep.* **5,** 15526 (2015).

36. Ondarçuhu, T. *et al.* Wettability of partially suspended graphene. *Sci. Rep.* **6,** 24237 (2016).